IEEE Trans. Electron Dev., vol. 69, no. 8, pp. 4064-4074, 2022

Methods for Extracting the Temperature and Power Dependent Thermal Resistance for SiGe and III-V HBTs from DC Measurements: A Review and Comparison Across Technologies

Markus Müller, Vincenzo d'Alessandro, Sophia Falk, Christoph Weimer, Xiaodi Jin, Mario Krattenmacher, Pascal Kuthe, Martin Claus and Michael Schröter

Abstract—Many different methods have been proposed in the literature for the extraction of the thermal resistance of heterojunction bipolar transistors (HBTs). This review presents a detailed evaluation and discussion of several widely used methods. Special emphasis is put on a generalized analysis of the underlying assumptions, suitable operating point range and necessary measurement effort of each method. The accuracy of each method is determined by applying it to data based on circuit simulations of advanced SiGe and III-V HBT technologies. Experimental data from those technologies are used to highlight practical issues. A guideline for the selection of the most suitable method in practice is also given.

Index Terms—compact modeling, heterojunction bipolar transistor, HBT, parameter extraction, self-heating, thermal resistance

I. Introduction

THE continuous demand for faster and more power-efficient devices and applications has led to shrinking dimensions of HBTs and, therefore, increasing current densities. At the same time lateral heat-spreading in SiGe HBTs has been restricted by the use of shallow and deep trenches or, in HBTs based on III-V semiconductors, by their mesa structure. In combination, these effects lead to severe self-heating in all modern technologies. The corresponding junction temperature rise impacts the terminal characteristics of HBTs. For this reason, self-heating needs to be consistently taken into account for both circuit design and compact model parameter extraction. Furthermore, predicting the safe-operating-area (SOA) of HBT technologies which are highly susceptible to thermal breakdown, like III-V HBTs, requires accurate modeling of self-heating.

The widely used compact models HICUM/L2 [1], MEXTRAM 504 [2], and VBIC [3, 4] take self-heating into account via an adjunct thermal network that contains a thermal resistance. Therefore, it is important to understand the underlying assumptions and resulting accuracy of the thermal resistance extraction methods. In this work, only methods for determining the thermal resistance from DC measurements are reviewed. In contrast to low-frequency AC or pulsed transient methods, DC measurements are easier to perform and require less expensive equipment. DC methods are thus attractive for practical parameter extraction tasks in an industrial environment. In the literature, many different methods for extracting the thermal resistance have been proposed [5–22], which can yield widely different results. However, a review of these methods that generalizes, compares and verifies them for different HBT technologies has not been presented so far. In particular, the operating point dependence of the extracted thermal resistance-related model parameters has rarely been investigated.

This manuscript is organized as follows. In Section II the thermal resistance models of industry-standard HBT models are reviewed. The investigated HBT technologies are introduced in Section III . Section IV highlights the importance of the Early-effect in the context of thermal resistance parameter extraction. Section V discusses the widely used extraction methods in a general way and applies them to the different technologies. Finally, Section VI provides a recommendation on selecting a thermal resistance parameter extraction method for practical purposes and discusses an improved implementation of the thermal resistance in compact models.

II. Thermal Resistance Modeling

Generally, the thermal resistance depends on the backside temperature of the chip T_B, and the power P_D dissipated in the transistor [23]. For junction temperatures in the range of 250...500 K, for which the existing standard compact models are valid, the thermal resistance can be described with sufficient accuracy by [23]

$$R_\mathrm{th}(T_\mathrm{B}, P_\mathrm{D}) = R_\mathrm{th}\left(T_\mathrm{B}\right)\left(1 + \alpha_\mathrm{Pd} P_\mathrm{D}\right) , \tag{1}$$

where [9, 13, 24]

$$R_\mathrm{th}(T_\mathrm{B}) = R_\mathrm{th,0}\left(\frac{T_\mathrm{B}}{T_0}\right)^{\zeta_\mathrm{th}} \tag{2}$$

Manuscript received April X, 20XX; revised August Y, 20YY.

M. Müller, S. Falk, C. Weimer, X. Jin, M. Krattenmacher and M. Schröter are with the Chair for Electron Devices and Integrated Circuits at TU Dresden, Germany. E-mail: markus.mueller3@tu-dresden.de

M. Müller, C. Weimer, X. Jin, P. Kuthe , M. Krattenmacher and M. Schröter are also with SemiMod GmbH, Dresden, Germany.

M. Claus and P. Kuthe are with Infineon Technologies AG, Neubiberg, Germany.

Vincenzo. d'Alessandro is with Department of Electrical Engineering and Information Technologies, University Federico II, Naples, Italy.

and $R_{\mathrm{th},0}$ is the thermal resistance at a reference temperature (e.g. $T_0 = 300\,\mathrm{K}$) and for negligible P_D. Eq. (2) models R_th as function of T_B only, using the temperature dependent analytical description of the thermal conductivity with the exponent factor $\zeta_\mathrm{th} > 1$. The second term in (1) takes into account a further change of the thermal conductivity (versus T_B) resulting from non-negligible P_D. The corresponding temperature coefficient is then approximated by

$$\alpha_\mathrm{Pd} \approx \zeta_\mathrm{th} R_\mathrm{th}(T_\mathrm{B}) / (2T_\mathrm{B}) > 0 \tag{3}$$

and results from a linearized representation of an originally non-linear dependence [23]. The junction temperature, required for modeling the impact of self-heating on the electrical device behavior in HBTs, is given by

$$T_\mathrm{j} = T_\mathrm{B} + R_\mathrm{th}(T_\mathrm{B}, P_\mathrm{D}) P_\mathrm{D}\,. \tag{4}$$

Compact models contain a simplified version of (1). In VBIC, R_th is assumed to be independent of temperature and power [3]. MEXTRAM 504 contains (2) and neglects the power dependent term of (1) [2] . HICUM/L2 accounts for the power related term, but in the modified form

$$R_\mathrm{th} = R_{\mathrm{th},0} \left(\frac{T_\mathrm{j}}{T_0}\right)^{\zeta_\mathrm{th}} \left[1 + \alpha_\mathrm{th}\,(T_\mathrm{j} - T_0)\right] \tag{5}$$

with $R_{\mathrm{th},0}$, $\alpha_\mathrm{th} > 0$ and $\zeta_\mathrm{th} > 0$ as model parameters. Note that the multiplicand $(T_\mathrm{j}/T_0)^{\zeta_\mathrm{th}}$ may cause numerical stability issues [13].

The compact R_th formulation of HICUM/L2 with $\zeta_\mathrm{th} = 0$ is related to (1), yet neglects an important term [13]. A comparison between TCAD generated reference data for $R_\mathrm{th}(P_\mathrm{D}, T_\mathrm{B})$ to least squares fits of the linearized (5) with $\zeta_\mathrm{th} = 0$ and the more rigorous model (1) with α_Pd as a model parameter is shown in Fig. 1. Evidently, (1) with α_Pd as a model parameter enables accurate compact modeling of $R_\mathrm{th}(P_\mathrm{D}, T_\mathrm{B})$.

The dissipated power is typically approximated by

$$P_\mathrm{D} = I_\mathrm{C} V_\mathrm{CE}\,, \tag{6}$$

where V_CE is the collector-emitter terminal voltage, and I_C is the collector terminal current. Since the actual power density is spatially distributed, one may question the accuracy of (6) as it represents the total externally applied power to the HBT structure. A somewhat improved expression that accounts for the power density just in the internal transistor has been employed in [7]. Since the calculation of the power relevant to the temperature increase is approximate in any way and (6) is computationally more efficient, it will be used herein. There has been evidence of the Peltier effect occurring in HBTs [20]. However, if existing, its impact on the junction temperature is small and included in the extracted value of R_th. The goal of this work is to evaluate widely used methods in terms of their accuracy for extracting the thermal resistance-related model parameters $R_{\mathrm{th},0}$, ζ_th and α_pD of (1).

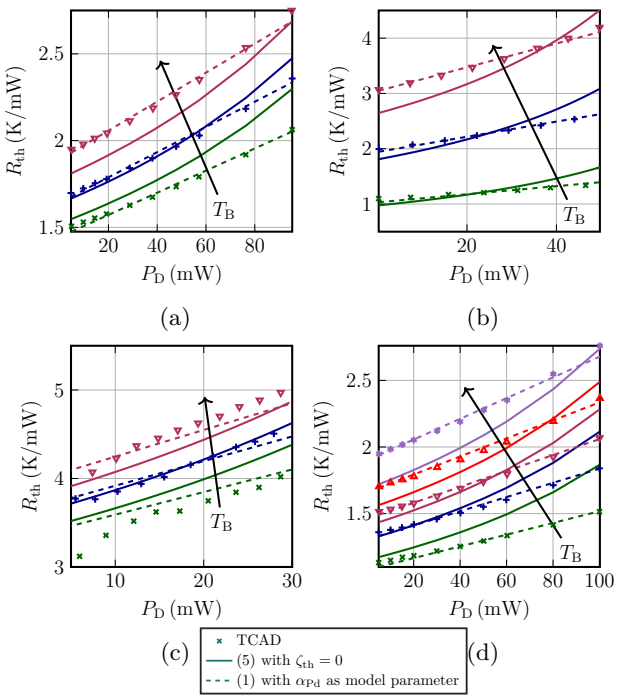

Figure 1: Least squares fit of linearized HICUM/L2 formulation (5) with $\zeta_\mathrm{th} = 0$ (solid lines) and (1) with α_Pd as a model parameter (dashed lines) to TCAD data (symbols) for $R_\mathrm{th}(P_\mathrm{D}, T_\mathrm{B})$ from (a) [25, Fig. 5(b)] at $T_\mathrm{B} = [300, 333, 373]\,\mathrm{K}$, (b) [23, Fig. 5] at $T_\mathrm{B} = [200, 300, 400]\,\mathrm{K}$, (c) [13, Fig. 52(f)] at $T_\mathrm{B} = [300, 325, 350]\,\mathrm{K}$ and (d) [26, Fig. 6(b)] at $T_\mathrm{B} = [233, 273, 300, 333, 373]\,\mathrm{K}$.

III. Investigated HBT Technologies

Including different process technologies enables to draw more general conclusions w.r.t. the practical suitability of the evaluated extraction methods. Table 1 provides an overview of the technologies investigated in this work, including 0.13 µm and 0.18 µm production SiGe BiCMOS technologies (from Infineon, IHP, Tower Semiconductor) as well as a 0.25 µm InP HBT process (Teledyne). For Infineon's B11 technology, both a high-speed (HS) and a medium-speed (MS) transistor flavor were considered. For each technology, a reference device has been selected with the corresponding parameters listed in Table 1. The model parameters have been extracted and verified using measurement data and a parameter extraction flow similar to the ones discussed in [27–29]. As no method for extracting α_Pd yielded reasonable results, this model parameter was tuned on output characteristics at very-high injection. Subsequently, only the technology names will be used.

IV. On the Influence of the Early-effect

Most of the investigated R_th extraction methods do not explicitly take a V_CB dependence of the collector current I_C into account. It is therefore important to understand under which conditions this assumption holds. For an HBT biased in forward active mode the collector current (without a possible contribution from the avalanche effect)

Technology	$f_T@V_{BC}=0\,V$ (GHz)	$f_{max}@V_{BC}=0\,V$ (GHz)	$R_{th,0}$ (K/mW)	α_{Pd} (W^{-1})	ζ_{th}	V_A (V)
IFX B11HS	250	370	3.6	4.2	0.92	>100
IFX B11MS	80	250	3.0	4.2	0.92	>100
IHP SG13G2	300	500	3.2	6.3	0.71	390
TJ SBC18H5	300	345	5.4	5.1	0.76	18
TSC250	370	650	1.7	2.1	0.88	40

Table I: Overview of the different technologies including their thermal resistance model parameters, transit frequencies f_T, maximum oscillation frequencies f_{max} and forward Early voltages V_A.

is given by the generalized integral charge-control relation [1]

$$I_C = \frac{c_{10}\left(T_j\right)}{Q_{pT}\left(V_{B'E'}, V_{B'C'}, T_j\right)} \exp\left(\frac{V_{B'E'}}{V_{Tj}}\right). \tag{7}$$

Here c_{10} is only a function of T_j, Q_{pT} is the bias and temperature-dependent weighted transport-related hole charge in the transistor, $V_{Tj} = k_B T_j/q$ the thermal voltage, and the primed nodes denote the terminals of the internal transistor. At low to medium injection, the V_{CB} dependence of I_C is caused by the Early-effect that enters (7) via the BC depletion charge within Q_{pT}. In the high injection region a modulation of the mobile charge in the collector leads to a V_{CB} dependence of I_C that can generally not be neglected. For large reverse BC voltages, a possible avalanche effect increases the dependence of I_C on V_{CB}. Therefore, R_{th} extraction methods should always be employed in the low to medium injection region, where the modulation of the mobile charge and the avalanche effect does not cause a V_{CB} dependence of I_C.

In the low- to medium-injection region, a reasonably accurate approximation of (7) is

$$I_C = I_S\left(T_j\right)\left(1+\frac{V_{CE}}{V_A}\right)\exp\left(\frac{V_{BE}}{m_C V_{Tj}}\right), \tag{8}$$

where $I_S\left(T_j\right)$ is the collector saturation current, V_A the forward Early-voltage, m_C a temperature independent non-ideality-factor, and V_{BE} the voltage between the external B and E terminal [30]. Therefore, the output conductance g_o can be approximated by

$$\frac{g_o}{I_C} = \frac{1}{V_A + V_{CE}} + \left.\frac{\mathrm{d}I_C}{\mathrm{d}T_j}\right|_{V_{BE},V_{CE}} R_{th}\,. \tag{9}$$

If the first term of (9) is negligible compared to the second one, the impact of a V_{CE} change on I_C is dominated by self-heating and neglecting the Early-effect is justified. The second term of (9) is proportional to I_C, hence the accuracy of methods that neglect the Early-effect will improve with higher I_C. However, when I_C becomes too large, high-current effects set in and (8) is no longer valid. Methods that do not consider a V_{CB} dependence of I_C must therefore have a sweet spot in the medium injection region, where the relative importance of the Early-effect is minimal compared to self-heating, while high-current effects are not yet relevant. Medium-speed transistor flavors have an earlier onset of high-current effects compared to their HS counterparts due to a lower collector doping. Their sweet spot must therefore be more narrow.

The output conductance g_o has been calculated from measurement data and is plotted in Fig. 2(a) to provide a feel for the relevance of the Early-effect in advanced technologies. Its importance can be estimated as follows: First one plots the normalized output conductance g_o/I_C versus I_C at constant V_{CE}. Then, if the y-axis intercept of a line fitted to the data at low to medium current densities (i.e. before the drop of the transit frequency) is small compared to the value of g_o/I_C in the operating range of interest for R_{th} extraction, the Early-effect can safely be neglected.

Further insight is obtained by plotting the ratio g_{el}/g_o, where $g_{el} = \left.\frac{\mathrm{d}I_C}{\mathrm{d}V_{CE}}\right|_{T_j}$. Based on accurate HICUM/L2 models g_{el} has been calculated, the results are shown in Fig. 2(b). For B11HS and SG13G2, the Early-effect can be neglected for a wide J_C range. For the other technologies, this is generally not the case.

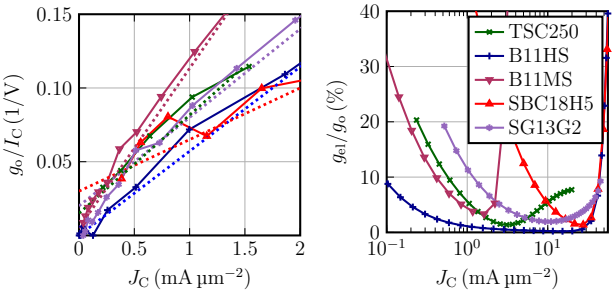

(a) (b)

Figure 2: (a) Measured normalized output conductance g_o as function of collector current density J_C (solid) and extrapolated lines as described in the text (dashed) at $V_{CE} = 1\,V$. (b) Relative contribution of the output conductance g_{el} due to the modulation of the charge to the total output conductance g_o at $V_{CE} = 1\,V$ from HICUM/L2 simulations.

V. Methods and Verification

Methods for obtaining the thermal resistance parameters from measured device characteristics are verified in this section using circuit-simulator-generated data based on scalable HICUM/L2 models. The models have been verified for a number of device geometries and are believed to accurately represent the physical properties of each technology. A similar methodology has also been successfully applied in previous works (e.g. [13, 31]).

Working with such synthetic "measurement" data allows evaluating the accuracy of parameter extraction methods since the target model parameters are known, which is not the case when working with measurement data. In principle, TCAD simulations could yield more insight compared to synthetic data because differential equations that describe carrier- and heat-transport are solved rigorously. However, representative TCAD simulations require extensive calibration of semiconductor transport equations

[32, 33] and the generation of a 3D simulation grid [16], owing to the fact that self-heating is a 3D effect. For the relatively large number of technologies investigated herein, a TCAD based approach is therefore not realistically feasible. Certain issues that arise in practice are exemplified using measured data.

When using synthetic data, the results can only be representative of reality if physical relations are employed for data generation. Hence, for generating the reference data herein, version 2.4.0 of the physics-based compact model HICUM/L2 has been employed, but using the more rigorous formulation (1) instead of (5) for ensuring as physical as possible synthetic data, see Section II. The circuit simulator ADS from Keysight has been employed for circuit simulation.

Some R_{th} extraction methods merely differ by using different measured device characteristics (e.g. [10, 12]), optimization approaches (e.g. [5, 7]) or model equations for the thermal resistance (e.g. [14, 15]). Hence, similar methods are grouped and analyzed together. The differences between such similar methods are briefly highlighted and only a carefully selected sub-set of the methods from each group is discussed. All methods have been implemented into the in-house parameter extraction tool DMT [34] that uses VerilogAE as a backend for accessing Verilog-A model equations [35]. The methods in [21, 22] are not considered here as they require a large measurement effort as well as time-consuming graphical solution methods that are difficult to implement into a parameter extraction program.

A. Intersection Method

a) Description: Methods for extracting the R_{th} model parameters from intersection points of the I_{C} vs. V_{BE} [8, 11, 12] or the I_{C} vs. V_{CE} characteristics [10] at different T_{B} have been proposed in the literature. A generalization for arbitrary thermal resistance models has been given in [13]. The fundamental assumption of these methods is that the collector current can be modeled as

$$I_{\mathrm{C}}\left(V_{\mathrm{BE}}, T_{\mathrm{j}}\right) = I_{\mathrm{S}} \exp\left(\frac{V_{\mathrm{BE}}}{m_{\mathrm{C}} V_{\mathrm{T_j}}}\right) . \tag{10}$$

Since (10) only depends on V_{BE} and T_{j}, operating points with different combinations of $(T_{\mathrm{B}}, P_{\mathrm{D}})$ but identical $(I_{\mathrm{C}}, V_{\mathrm{BE}}, T_{\mathrm{j}})$ exist. Each of those intersection points yields

$$T_{\mathrm{B},1} + R_{\mathrm{th}}(T_{\mathrm{B},1}, P_{\mathrm{D},1}) P_{\mathrm{D},1} = T_{\mathrm{B},2} + R_{\mathrm{th}}(T_{\mathrm{B},2}, P_{\mathrm{D},2}) P_{\mathrm{D},2} . \tag{11}$$

For n intersection points one obtains n such equations that can be solved for the R_{th} model parameters either analytically [10, 12] or, depending on the size of the equation system, its conditioning, and the number of model parameters to be solved for, by numerical methods. It is noteworthy that, in principle, intersection points can be determined from any electrical quantity that depends only on V_{BE} and T_{j}.

b) Validity: The validity conditions for (10), being a function of V_{BE} and T_{j} only, can be found by comparing (10) to (7):

(i) Early- and high-injection effects need to be negligible.
(ii) The internal BE voltage needs to equal the external one.

Condition (i) has been discussed in Section IV. Condition (ii) is fulfilled if the voltage drop across the base resistance R_{B} and emitter resistance R_{E} is negligible, e.g. $I_{\mathrm{B}} R_{\mathrm{B}} \ll V_{\mathrm{T_j}}$ and $(I_{\mathrm{C}} + I_{\mathrm{B}})\, R_{\mathrm{E}} \ll V_{\mathrm{T_j}}$, with I_{B} as base current.

Condition (ii) may be relaxed by using

$$V_{\mathrm{B'E'}} = V_{\mathrm{BE}} - (I_{\mathrm{C}} + I_{\mathrm{B}})\, R_{\mathrm{E}} - I_{\mathrm{B}} R_{\mathrm{B}} \tag{12}$$

instead of V_{BE} in (10). For applying (11) it is sufficient that the difference between internal and external BE voltage, ΔV_{BE}, does not vary significantly between $T_{\mathrm{B},1}$ and $T_{\mathrm{B},2}$.

c) Application: In [12] $I_{\mathrm{C}}\left(V_{\mathrm{BE}}\right)$ characteristics at different V_{CE} are used to determine intersection points. The work in [10] employs output characteristics at forced I_{B}. Here, $I_{\mathrm{C}}\left(V_{\mathrm{BE}}\right)$ characteristics at different V_{CB} are used instead. It does not matter from which curves intersection points are determined as long as the transistor is operated in forward active mode. Hence, when using $I_{\mathrm{C}}\left(V_{\mathrm{BE}}\right)$ characteristics at forced V_{CE} or V_{CB} one must pay attention that $\exp(V_{\mathrm{BE}}/V_{\mathrm{T}}) \gg \exp(V_{\mathrm{BC}}/V_{\mathrm{T}})$ at the intersection point. Depending on the selected bias and temperature range, there may exist different intersection points. For B11HS Fig. 3 (a) depicts examples for unsuitable intersection points as they occur at current densities in the high-injection region, that is around and beyond $J_{\mathrm{C}}(f_{\mathrm{T,peak}})$, where (10) is not valid. For III-V and MS HBTs, intersection points are more difficult to measure due to an earlier onset of high-current effects and a smaller SOA as compared to HS SiGe HBTs. For TSC250 and B11MS, the measured backside temperatures for determining intersection points should differ by no more than 5 K, as depicted in Fig. 3 (b) for TSC250. For the HS SiGe HBT technologies investigated herein, a temperature difference of 10 K suffices to find useful intersection points.

For determining the best operating point range of the intersection method, the following experiment is performed on synthetic data. With α_{pD} and ζ_{th} fixed to their reference values, $R_{\mathrm{th},0}$ is extracted from the intersection points of two $I_{\mathrm{C}}\left(V_{\mathrm{BE}}\right)$ characteristics at $(T_{\mathrm{B},1}, V_{\mathrm{CB},1} = -\Delta V_{\mathrm{CB}}/2)$ and $(T_{\mathrm{B},2}, V_{\mathrm{CB},2} = \Delta V_{\mathrm{CB}}/2)$ while ΔV_{CB} is varied. The results of this experiment are displayed in Fig. 4. For small ΔV_{CB} values the current density at the intersection point may be quite large and (10) becomes invalid, as discussed in Section IV. For large ΔV_{CB} values, the avalanche effect and saturation may invalidate condition (i). It can be concluded that the intersection points used for parameter extraction should be selected such that the point at the lower T_{B} has the highest possible V_{CB} that does not cause impact ionization. The point at the higher T_{B} should have the lowest possible V_{CB} that does not cause the transistor to enter saturation.

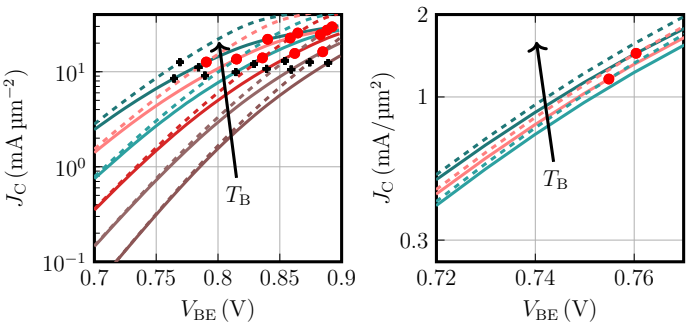

(a) (b)

Figure 3: Example for intersection points (red circles) from measurement data of (a) B11HS and (b) TSC250. In (a) T_B is swept from 298 K to 423 K in 25 K steps and in (b) from 298 K to 308 K in 5 K steps. For each T_B, two V_{CB} voltages equal to (a) 0.3 V (dashed lines), −0.3 V (dashed lines) and (b) 0.5 V (solid lines), −0.3 V (solid lines) are shown. In (a) $J_C(f_{T,peak})$ is indicated by black crosses. All intersection points in (a) are not suitable for the intersection method as discussed in the text.

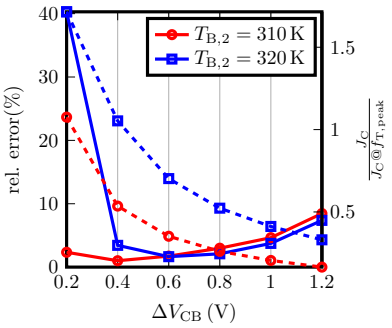

Figure 4: Relative error of the extracted thermal resistance R_{th} of B11HS (left y-axis, solid lines) and normalized collector current density at the intersection point (right axis, dashed lines) from two $I_C(V_{BE})$ characteristics with $V_{CB,2} = -\Delta V_{CB}/2$, $V_{CB,1} = \Delta V_{CB}/2$ and $T_{B,1} = 300$ K as described in the text. The current density is normalized to the current density $J_{C,peak} = J_C(f_T = f_{T,peak})$ at $V_{CB} = 0$ V.

As can be seen in Fig. 3 and Fig. 4, the difference in T_B between the characteristics used for determining intersection points influences the maximum V_{CB} for the characteristics at the higher T_B. The difference between $T_{B,1}$ and $T_{B,2}$ does not have a direct impact on the method's accuracy as long as conditions (i) and (ii) are met. This insight is beneficial because in practice T_B is not known exactly due to the limited temperature stability of the thermochuck.

The method has been applied to synthetic data of all technologies, Fig. 5 summarizes the determined accuracy. $I_C(V_{BE})$ characteristics at two different T_B, as documented in the caption of Fig. 5, were used to determine intersection points.

For B11HS and SG13G2 the accuracy for $R_{th,0}$ and ζ_{th} is better than 10 %. The accuracy is, in general,

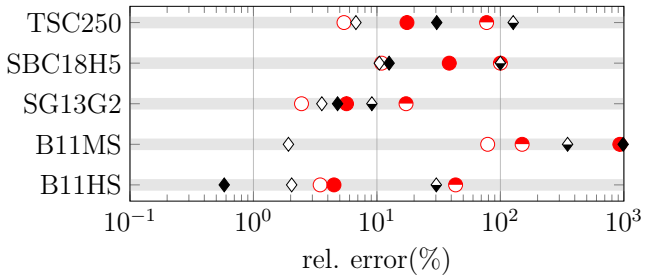

Figure 5: Relative error (in %) of $R_{th,0}$ (open symbols), ζ_{th} (filled symbols) and α_{pD} (half filled symbols) from the intersection method for different technologies as described in the text. The parameters were extracted using intersection points at $[(300, 310), (310, 320), (300, 320)]$ K (circles), and $[(300, 310), (340, 350), (370, 380)]$ K (diamonds). $V_{CB,1} = 0.2$ V and $V_{CB,2} = -0.2$ V.

significantly worse for B11MS, SBC18H5 and TSC250. For these technologies the intersection points for the chosen T_B grid occur at current densities where (10) does not hold and the V_{CB} dependence of the transfer current cannot be neglected (see Table 1 and Fig. 2(b)). In particular, both TSC250 and B11MS require a finer T_B grid for finding useful intersection points. Generally, ζ_{th} can be extracted quite accurately, however this is not the case for α_{pD}. Even slight inaccuracies of (10) lead to large extraction errors for this parameter.

In summary, the intersection method offers excellent accuracy for determining $R_{th,0}$ and ζ_{th}, provided that assumptions (i)-(ii) are met. Also, the intersection method is insensitive to the emitter resistance. However, several problems may occur in practice. For some III-V technologies, the current densities at the intersection points may be difficult to reach due to the SOA limits. Obtaining sufficiently accurate R_{th} model parameters requires measurements for at least four, better six, different T_B.

B. Methods Based on a Linearized Electrical Quantity

a) Description: Several methods have been proposed that employ a linearized electrical quantity as a temperature sensor [14–17]. These methods assume that a specific electrical quantity can, under certain operating conditions, be modeled as a linear function of the junction temperature. For example, choosing V_{BE} results, according to [14], in

$$V_{BE}(T_j) = V_{BE,0} + \left.\frac{dV_{BE}}{dT_j}\right|_{I_E} (T_j - T_{j,0}) \,. \qquad (13)$$

Here, $V_{BE,0}$ is the value of V_{BE} at the reference junction temperature $T_{j,0} = T_{B,0} + P_{D,0}R_{th}(T_{j,0}, P_{D,0})$ with $P_{D,0}$ as the power dissipation at the reference operating point. (13) is a model equation for the sensor with the unknowns $V_{BE,0}$, $\frac{dV_{BE}}{dT_j}$ and the model parameters of the employed $R_{th}(T_j, P_D)$ relation. The unknowns can be found by fitting (13) to experimental data at several (T_B, P_D) around $(T_{B,0}, P_{D,0})$. The work in [14] uses $R_{th}(T_j, P_D) = R_{th,00}$ and either I_C or V_{BE} as temperature sensor at fixed I_B

or fixed I_E. The data in [14] indicate that choosing V_BE as a sensor is most accurate. The method from [15] builds upon [14] by including a linear temperature dependence $R_\mathrm{th} = R_\mathrm{th,00}\left[1 + \alpha_\mathrm{th,0}\left(T_\mathrm{j} - T_\mathrm{j,0}\right)\right]$ with I_C as the sensor. This results in (see (9) in [15])

$$I_\mathrm{C}\left(T_\mathrm{B}, P_\mathrm{D}\right) = I_\mathrm{C,0} + \frac{\mathrm{d}I_\mathrm{C}}{\mathrm{d}T_\mathrm{j}}\left[\frac{T_\mathrm{B} - T_\mathrm{B,0} + R_\mathrm{th,00}\left(P_\mathrm{D} - P_\mathrm{D,0}\right)}{1 - \alpha_\mathrm{th,0} R_\mathrm{th,00} P_\mathrm{D}}\right], \tag{14}$$

which is adjusted to measurements by optimization, thereby allowing to determine $R_\mathrm{th,00} = R_\mathrm{th}(T_\mathrm{B,0}, P_\mathrm{D,0})$. The method in [14] has been slightly modified in [9] by using a quadratic instead of a linear temperature dependence of V_BE on T_j and an improved $R_\mathrm{th}(T_\mathrm{j}, P_\mathrm{D})$ relation.

Another enriched variant of the method in [14] has been proposed in [16], where V_BE is used as sensor at fixed I_E. It is shown that in the absence of Early, high-injection and avalanche effects the change of V_BE with T_j at fixed I_E can be modeled by

$$\left.\frac{\mathrm{d}V_\mathrm{BE}}{\mathrm{d}T_\mathrm{j}}\right|_{I_\mathrm{E}} = -\phi_0 + m_\mathrm{cf}\frac{k_\mathrm{B}}{q}\ln\left[\frac{I_\mathrm{C}}{I_\mathrm{S}\left(T_\mathrm{B,0}\right)}\right], \tag{15}$$

where ϕ_0 is a model parameter, m_cf is the collector current non-ideality-factor and $I_\mathrm{S}\left(T_\mathrm{B,0}\right)$ is the saturation current at the reference backside temperature of the chip [16]. For extracting the parameters of R_th the method proceeds as follows.

First, the parameters m_cf and $I_\mathrm{S}\left(T_\mathrm{B,0}\right)$ are extracted from transfer characteristics at low injection and $T_\mathrm{B,0}$. Second, forced I_E measurements at low injection ($T_\mathrm{j} \approx T_\mathrm{B}$) but different T_B are performed for extracting ϕ_0. Finally, measurements at forced I_E and swept V_CB are performed at $T_\mathrm{B,0}$ in the medium injection region, where self-heating is relevant, but (15) still holds. R_th can then be extracted from the slope of the V_BE-V_CB characteristics as

$$R_\mathrm{th}(T_\mathrm{B0}) = \frac{|\gamma|}{\left(|\gamma| - 1\right) I_\mathrm{E}\left.\frac{\mathrm{d}V_\mathrm{BE}}{\mathrm{d}T_\mathrm{j}}\right|_{I_\mathrm{E}}}, \tag{16}$$

where

$$\gamma = \left.\frac{\mathrm{d}V_\mathrm{BE}}{\mathrm{d}V_\mathrm{CB}}\right|_{I_\mathrm{E}} \tag{17}$$

and (15) is used to calculate $\left.\frac{\mathrm{d}V_\mathrm{BE}}{\mathrm{d}T_\mathrm{j}}\right|_{I_\mathrm{E}}$.

By repeating the procedure for several $T_\mathrm{B,0}$ the parameter ζ_th can be extracted from the obtained $R_\mathrm{th}(T_\mathrm{B})$ data. However, the parameter α_Pd cannot be extracted using this approach. The unique advantage of this method is that the temperature coefficient of the sensor is extracted using a physics-based equation at low-injection levels (see section III. D of [16]).

b) Validity: It is implicitly assumed that the selected sensor variable

(i) can be well approximated as a linear function of T_j and

(ii) does not depend on V_CB via electrical feedback.

For I_C and I_B the validity of (i) is difficult to evaluate due to the involved physics necessary to accurately model them as a function of T_j. In [15] it is suggested to measure the sensor variable as a function of T_B at low P_D for validating (i). However, a linear dependence of the sensor variable on T_B in the low- injection region does not prove the validity of (i) at higher injection and P_D. Based on synthetic data, assumption (i) is tested in Fig. 6 by directly plotting the sensor as a function of T_j at different T_B. Clearly $V_\mathrm{BE}\left(T_\mathrm{j}\right)$ is more linear than $I_\mathrm{C}\left(T_\mathrm{j}\right)$.

A physics-based explanation for the linearity of V_BE has been given in [16], which was also discussed in [36, 37] for silicon-on-glass BJTs. Regardless of the technology, V_BE is always more linear and has a lower dynamic range than I_C. Assumption (ii) has been discussed in Section IV.

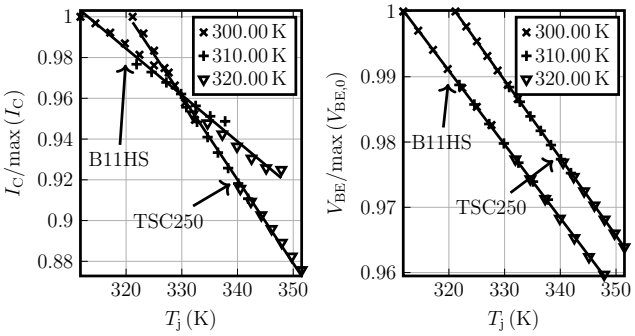

(a) (b)

Figure 6: Dependence of (a) I_C and (b) V_BE at fixed I_B on T_j for different T_B for B11HS and TSC250. Black solid lines resemble a linear fit of (13) to the simulated sensor variable vs. T_j; $J_\mathrm{B} = 17.7\,\mathrm{\mu A\,\mu m^{-2}}$ for B11HFC and $J_\mathrm{B} = 124\,\mathrm{\mu A\,\mu m^{-2}}$ for TSC250.

c) Application: The application of the method is described in detail in [15]. Eq. (13) is adjusted to several groups of measurement data of the sensor for extracting a value $R_\mathrm{th,00}$ at several $(T_\mathrm{B,0}, P_\mathrm{D,0})$. This can be done by either graphical or numerical methods. Finally, the R_th model parameters are determined by fitting (1) to the obtained $R_\mathrm{th,00}\left(T_\mathrm{B,0}, T_\mathrm{j,0}, P_\mathrm{D,0}\right)$ data. Figure 7 depicts typical results of fitting the sensor variable V_BE for two T_B values at fixed I_E.

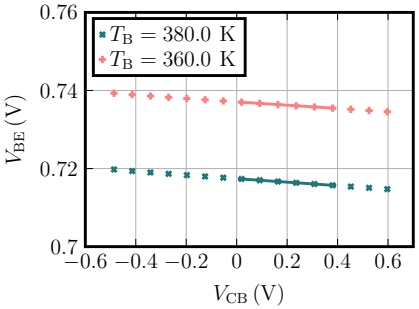

Figure 7: Fit of (13) (solid lines) with V_BE as sensor to measurement data (symbols) of B11HS at different T_B and $J_\mathrm{E} = 1.8\,\mathrm{mA\,\mu m^{-2}}$.

To investigate the operating point dependence of the extraction result, $R_\mathrm{th,0}$ is extracted while α_pD and ζ_th are fixed to their reference values from Table I and I_B

is varied. The results in Fig. 8 show that the accuracy of the method is strongly operating point dependent. A sweet spot as described earlier exists. Again, the method should not be applied too far in the high-current region, namely beyond $J_C\,(f_{T,peak})$.

The method has been applied to all reference technologies using different combinations of sensor and fixed variables, Fig. 9 summarizes the results. Here, (13) has been separately optimized for $T_B = [300, 310]$ K and $T_B = [370, 380]$ K and several $P_{D,0}$ to obtain $R_{th}(T_j, P_D)$ from five extracted $R_{th}(T_{j,0}, P_{D,0})$ points. The method has also been applied as described in the previous section and in [16], corresponding results are shown in Fig. 10. The average collector current density of the operating points in Fig. 9 and Fig. 10 is in the range $J_C = 1...5\,\mathrm{mA\,\mu m^{-2}}$ for all technologies.

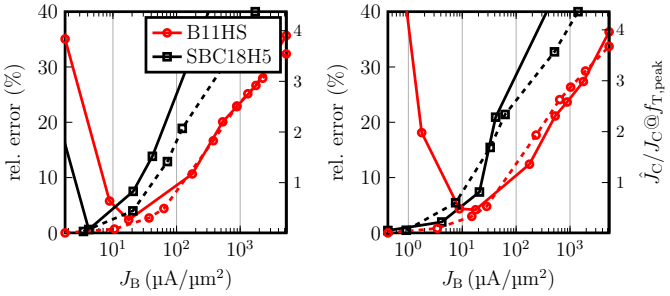

(a) (b)

Figure 8: Relative error of the extracted thermal resistance R_{th} for B11HS and SBC18H5 (left y-axis, solid lines) and normalized mean collector current density at $T_B = 300$ K in the operating point range used for optimizing (13) (right y-axis, dashed lines) with V_{BE} as temperature sensor at constant J_B and (a) $T_B = [300, 320, 340]$ K , (b) $T_B = [300, 305, 310]$ K.

According to Fig. 9 choosing V_{BE} as sensor variable is the best choice as it yields overall more accurate results for $R_{th,0}$ and ζ_{th} for all investigated technologies. This is attributed to the high linearity of V_{BE} [16]. More accurate extraction results can be obtained by accounting for the Early-effect [17]. One should not use (14) to model measurement data at T_B that vary more than ≈ 80 K as the assumed linearity of the sensor decreases for such a wide T_B range. The parameter α_{pD} can not be reliably extracted with this group of methods.

C. Simultaneous R_E and R_{th} Extraction Methods

a) Description: Several authors have noticed that the independent extraction of R_{th} is difficult as it impacts the terminal characteristics in a similar bias range as R_E [5–7]. The combined extraction of R_{th} and R_E has been suggested to overcome this issue by employing the base current formulation

$$I_B = I_{BEs}\,(T_j)\left[\exp\left(\frac{V_{B'E'}}{m_{BE}V_{Tj}}\right) - 1\right] \qquad (18)$$

together with

$$V_{B'E'} \approx V_{BE} - I_C R_E\,(T_j)\ . \qquad (19)$$

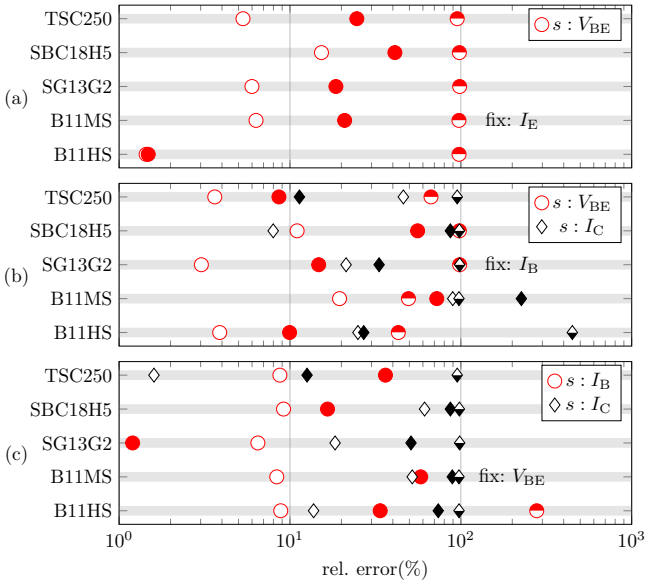

Figure 9: Relative error (in %) of $R_{th,0}$ (open symbols), ζ_{th} (filled symbols) and α_{pD} (half filled symbols) extracted from synthetic data using (13) with different combinations of fixed electrical variable and temperature sensor ("s:..."). (13) was separately optimized for $T_B = [300, 310]$ K and $T_B = [370, 380]$ K to obtain the model parameters as described in the text.

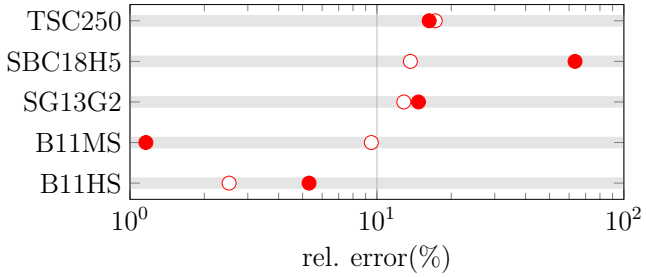

Figure 10: Relative error (in %) of $R_{th,0}$ (open symbols), ζ_{th} (filled symbols) from the linearized electrical quantity method after [16] using V_{BE} as sensor at fixed I_E for different technologies as described in the text.

The model parameters for $I_{BEs}\,(T_j)$ and m_{BE} are determined from measurements in bias regions with negligible self-heating and different T_B. All published methods assume $R_{th} = R_{th,00}\,[1 + \alpha_{th,0}\,(T_B - T_0)]$, i.e. no dependence of R_{th} on P_D. However, as will be explained later, one may use any $R_{th}(T_j, P_D)$ relation when numerical optimization is employed.

In [5], (19) is inserted into (18) for deriving a model for I_B as a function of T_j and V_{BE}, and therefore also of R_E, $R_{th,0}$ and α_{th}. The latter model parameter is, however, neglected in older publications. An analytical iterative procedure for determining $R_{th,0}$ and R_E is presented in [5]. In [6] a related method is proposed that uses similar model equations but, instead of determining $R_{th,0}$ and R_E from the base current, the linearized temperature coefficient of V_{BE} is analyzed. It is claimed that the main advantage of this method is that this coefficient is device-

geometry independent. Thus, $R_{\mathrm{th},0}$ can be obtained from measurements at only one temperature, provided that the temperature coefficient of V_{BE} is known. Most recent work in this category of methods has been conducted in [7], where similar assumptions compared to [5] are employed. In [7] it is recommended to determine the desired model parameters from output characteristics using a novel optimization strategy. None of the methods explicitly take α_{pD} or ζ_{th} into account. However, [7] suggests to determine $R_{\mathrm{th},0}$ at several T_{B} and then fit ζ_{th} using the extracted $R_{\mathrm{th},0}\,(T_{\mathrm{B}})$ relation. This procedure is not suitable for determining α_{pD}.

b) Validity: The simultaneous methods assume that

(i) the base current in forward active operation can be modeled by (18);
(ii) the voltage drop over the base resistance is negligible;
(iii) the P_{D} dependence of R_{th} is negligible.

Assumption (i) is technology-dependent and can be verified in practice by measurements. Several physical effects may give rise to non-ideal base current behavior and may invalidate this assumption [1]. Assumption (ii) can be checked if the base resistance is known. The last assumption (iii) is valid if the change of R_{th} with P_{D} is negligible. This assumption may be ensured by choosing a bias range with small, but non-negligible, self-heating. Notice that, in contrast to all other groups, this group of methods does not require I_{C} to be independent of V_{CB}.

c) Application: Numerical optimization of (18), (19) and (11) with $R_{\mathrm{E}} = (T_{\mathrm{j}}/T_0)^{\zeta_{\mathrm{re}}}$ to fit the measured base current at different V_{BE}, V_{CE} and T_{B}, yields a set of self-consistent model parameters.[1] Examples for the application of this method are shown in Fig. 11. The sensitivity of the method to the selected operating point range is analyzed in Fig. 12. For low J_{B}, self-heating is not relevant and the extracted $R_{\mathrm{th},0}$ is inaccurate. At too high J_{B}, the accuracy depends on the impact of the different base current components. For SG13G2, the perimeter component starts to play a role, while for SBC18H5 the BC barrier recombination causes deviations from (18).

Based on synthetic data, different extraction strategies have been evaluated. First, the strategy proposed in [7] was used for determining R_{th} and R_{E} for each T_{B} and then (2) was fitted to the resulting $R_{\mathrm{th}}(T_{\mathrm{B}})$ and $R_{\mathrm{E}}\,(T_{\mathrm{B}})$ curve. As alternative, all model parameters were optimized simultaneously from the base current at different V_{BE}, V_{CB} and T_{B}, using the full $R_{\mathrm{th}}(T_{\mathrm{j}}, P_{\mathrm{D}})$ relation (1) when calculating T_{j}. Here, as opposed to the original formulation [5, 7], all dependencies of R_{th} were consistently taken into account. The results are shown in Fig. 13 for R_{th} and in Fig. 14 for R_{E}. Quite accurate values for $R_{\mathrm{th},0}$ and ζ_{th} are obtained for all technologies, regardless of the chosen optimization strategy. The accuracy of the results varies for α_{pD} since it is quite sensitive to inaccuracies of (18). Provided that the base current is well approximated

[1]This generalized approach is used here as it allows to employ a generic numerical optimizer.

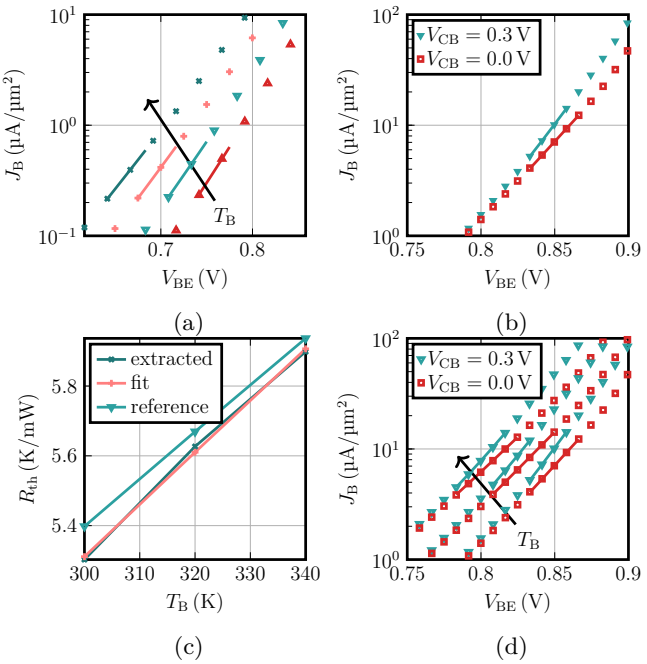

Figure 11: Application of the simultaneous R_{E} and R_{th} method to SBC18H5. (a) Comparison between diode model (18) (dashed lines) and measured I_{B} (symbols) for $V_{\mathrm{CB}} = 0\,\mathrm{V}$ and $T_{\mathrm{B}} = [300, 320, 340, 360]\,\mathrm{K}$ in the low injection region, where self-heating is negligible. (b) Fit of (18) with (19) (dashed lines) to the measured I_{B} (symbols) at different V_{CB} and $T_{\mathrm{B}} = 300\,\mathrm{K}$. (c) Extracted $R_{\mathrm{th}}(T_{\mathrm{B}})$ from optimization at each T_{B}. (d) Fit of (18) with (19) (dashed lines) to the measured I_{B} (symbols) simultaneously at different V_{CB} and $T_{\mathrm{B}} = [300, 320, 340]$ K. Solid lines indicate the bias region used for model parameter extraction. In (b) and (d) only two of the fixed $V_{\mathrm{CB}} = [0.3, 0.2, 0.1, 0]$ V lines used for optimizing (19) are shown.

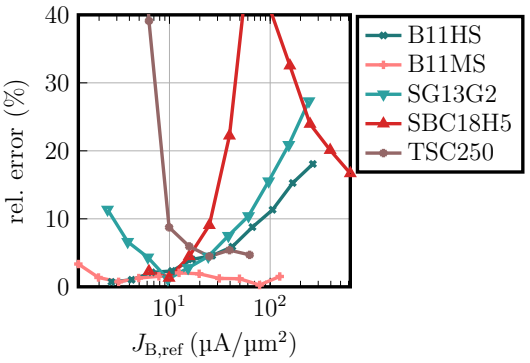

Figure 12: Relative error (in %) of the extracted $R_{\mathrm{th},0}$ from the simultaneous R_{E} and R_{th} method as a function of the J_{B} range used for optimization and assuming $R_{\mathrm{th}} = R_{\mathrm{th},0}$. The J_{B} range used for extraction of $R_{\mathrm{th},0}$ was taken from the $J_{\mathrm{B}}\,(V_{\mathrm{BE}})$ characteristics in the range 0.5...1.5 times a reference value $J_{\mathrm{B,ref}}$ and $V_{\mathrm{CB}} = [0.2, 0.1, 0, -0.1]$ V at $T_{\mathrm{B}} = 300\,\mathrm{K}$. At least 12 discrete operating points were used for the optimization.

by (18), the simultaneous methods can provide excellent accuracy and also give very accurate values for R_E [31].

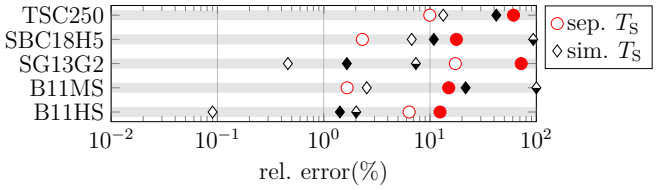

Figure 13: Relative error of $R_{\mathrm{th},0}$ (open symbols), ζ_th (filled symbols) and α_pD (half filled symbols) extracted with the simultaneous method either using optimization separately at each T_B or simultaneously at all T_B. Data used for extraction were taken at $T_\mathrm{B} = [300, 320, 340]$ K, $V_\mathrm{CB} = [0.3, 0.2, 0.1, 0, -0.1]$ V and a J_B range of 9...32 mA µm^{-2} (B11HS, B11MS), 15...154 mA µm^{-2} (SG13G2), 4...15 mA µm^{-2} (SBC18H5) and 40...70 mA µm^{-2} (TSC250).

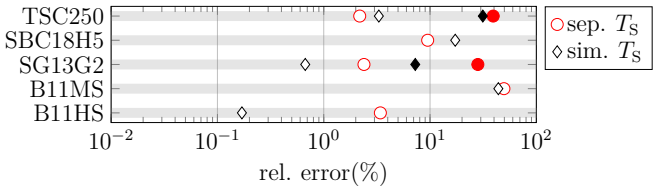

Figure 14: Relative error of R_E (open symbols) and ζ_re (filled symbols) extracted with the simultaneous method either using optimization separately at each T_B or simultaneously at all T_B. Same data as used for obtaining the results in Fig. 13. For B11MS, B11HS and SBC18H5 $\zeta_\mathrm{re} \approx 0$ and, therefore, the relative error for this parameter is not shown.

D. Differential Methods

a) Description: Methods for extracting R_th from a first-order Taylor expansion of an electrical sensor X have been proposed in the literature [18, 19]. The underlying model equation for these methods is (13), i.e. the same equation as for the methods that rely on a linearized electrical quantity. In contrast to those methods, the differential methods apply (13) just in a small region around each operating point. The thermal resistance can be directly computed from the derivatives of X as

$$R_\mathrm{th} = \left(\left.\frac{\mathrm{d}X}{\mathrm{d}P_\mathrm{D}}\right|_{T_\mathrm{B}} \right) / \left(\left.\frac{\mathrm{d}X}{\mathrm{d}T_\mathrm{B}}\right|_{P_\mathrm{D}} \right) , \tag{20}$$

which is the generalized version of (4) in [19]. Similarly, the generalized version of (7) in [18] reads

$$R_\mathrm{th} = \frac{\left.\frac{\mathrm{d}X}{\mathrm{d}V_\mathrm{CE}}\right|_{T_\mathrm{B}}}{\left.\frac{\mathrm{d}X}{\mathrm{d}T_\mathrm{B}}\right|_{V_\mathrm{CE}}} \frac{1}{I_\mathrm{C}\left(1 + V_\mathrm{CE}/V_\mathrm{A}\right)} . \tag{21}$$

Eqs. (20) and (21) are derived in the Appendix. Derivatives of X w.r.t. to V_CE due to electrical feedback, i.e. the Early-effect, are only partially taken into account.

b) Validity: The differential methods are based on the same assumptions as the methods that rely on a linearized quantity. The assumption of a linear T_j dependence is justified if changes in T_j are sufficiently small. In practice, the minimum change of T_j used to calculate the derivatives in (20) and (21) is limited by the temperature stability of the thermal chuck and the justifiable effort for measurements with a sufficiently fine temperature grid.

c) Application: Eq. (20) is ideally evaluated from output characteristics. First T_B is changed by ΔT_B while P_D is kept constant via adjusting V_CE. Then, P_D is changed by ΔP_D while T_B is kept constant. Eq. (21) is evaluated by first changing T_B by ΔT_B while V_CE is kept constant. Then, V_CE is changed by ΔV_CE while T_B is kept constant. By repeating this procedure at several V_CE and T_B one obtains $R_\mathrm{th}(T_\mathrm{B}, P_\mathrm{D})$ as shown in Fig. 15. From fitting the data in Fig. 15(b), the model parameters of (1) are determined.

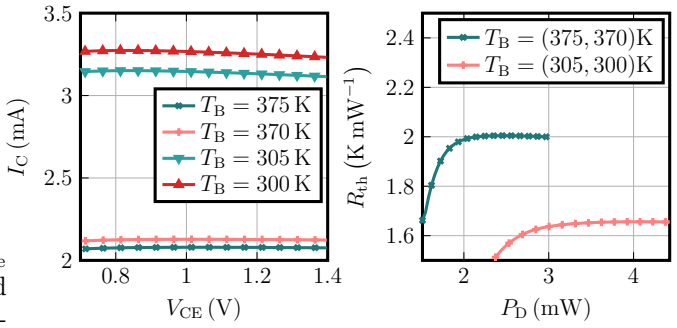

Figure 15: Application of the differential R_th extraction method from [18] to TSC250. (a) Output characteristics at $J_\mathrm{B} = 40$ µA µm^{-2} for applying (21). (b) Resulting $R_\mathrm{th}(T_\mathrm{B}, P_\mathrm{D})$ from (21).

In [18] $X = I_\mathrm{B}$ at fixed V_BE is proposed, while [19] uses $X = I_\mathrm{C}$ or $X = V_\mathrm{BE}$ at fixed I_B. Note that at fixed I_B the choices $X = I_\mathrm{C}$ or $X = \beta$ are mathematically equivalent. The derivation in the Appendix shows that there are no restrictions w.r.t. to the chosen fixed quantity, i.e. both fixed V_BE and I_B can be used.

Eqs. (20) and (21) have been applied to the different technologies with all combinations of X. The results are shown in Fig. 16 for fixed I_B and in Fig. 17 for fixed V_BE. For the considered technologies, the best results were obtained using $X = V_\mathrm{BE}$ with fixed I_B; differences between using (20) or (21) are insignificant. It is recommended to use (21) in practice since its evaluation does not require interpolation, provided that the same operating points are measured at all T_B. The operating point dependence of the extraction result is displayed in Fig. 18. The method should not be applied far beyond $f_\mathrm{T,peak}$. The differential methods show a high accuracy for $R_{\mathrm{th},0}$ and ζ_th when applied to simulation data, though α_pD can not be determined reliably. In practice, the accuracy of the differential methods is significantly impacted by unavoidable noise in measurement data as visualized in Fig. 19. Also, they require a high measurement effort.

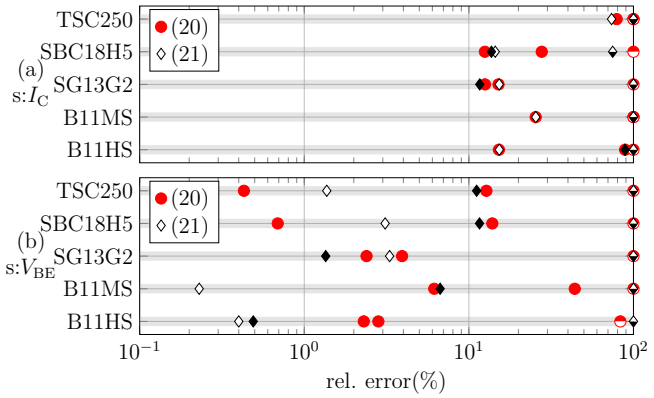

Figure 16: Relative error of extracted $R_{th,0}$ (open symbols), ζ_{th} (filled symbols) and α_{pD} (half filled symbols) from differential methods at fixed I_B. I_B has been selected at all temperatures such that the average J_C of the output characteristics is in the medium injection region. The temperature pairs used to evaluate the differentials in (20) and (21) were $T_B = [300, 310]$ K and $T_B = [370, 380]$ K.

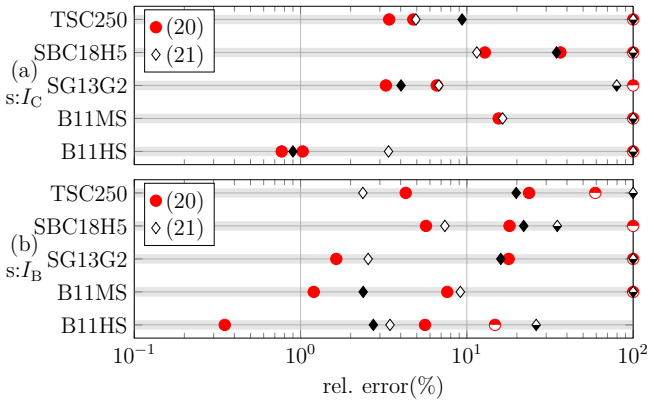

Figure 17: Relative error of extracted $R_{th,0}$ (open symbols), ζ_{th} (filled symbols) and α_{pD} (half filled symbols) from differential methods at fixed I_B. I_B has been selected at all temperatures such that the average J_C of the output characteristics is in the medium injection region. The temperature pairs used to evaluate the differentials in (20) and (21) were $T_B = [300, 310]$ K and $T_B = [370, 380]$ K.

VI. Method Selection in Practice and Implementation into a Compact Model

The results presented above allow to draw the following conclusions regarding method selection in practice, which is visualized in Fig. 20. The intersection method offers excellent accuracy if the Early-effect is negligible, which can be checked using (9). In particular, these methods appear to be most suitable to extract α_{Pd}.

If the Early-effect is relevant, the simultaneous method is recommended in case I_B can be modeled by a single diode equation. If this is not the case, a linearized electrical quantity method using V_{BE} as a sensor may give reasonable results. Differential methods are not recommended in practice since the derivatives in (20) and (21) obtained from measurement data may be too noisy.

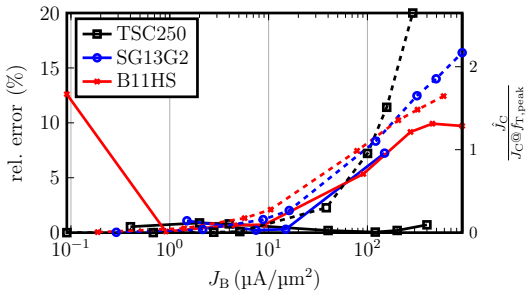

Figure 18: Operating point dependence of the relative error (in %) of the extracted $R_{th,0}$ with ζ_{th} and α_{pD} fixed to their reference values using (21) with $X = V_{BE}$ (solid lines) and the normalized average collector current density (dashed lines). $R_{th,0}$ has been extracted by fitting (1) to $R_{th}(P_D)$ calculated from (21) based on output characteristics at forced J_B and $T_B = 300$ K.

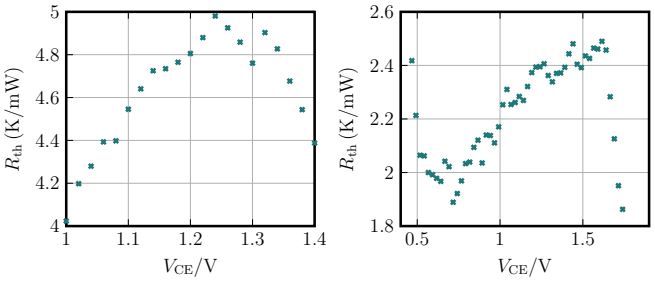

Figure 19: Application of the differential method (20) with fixed I_B and V_{BE} as sensor to measurement data for (a) SBC18H5 and (b) TSC250 at $T_B = [298, 308]$ K.

It has to be mentioned that the R_{th} value obtained from transistor measurements always contains a non-negligible contribution from the upward heat-flow across the metal connection to the pads. Therefore, R_{th} will be higher in an actual IC. To remove the pad influence on R_{th}, a special set of test structures is required [38].

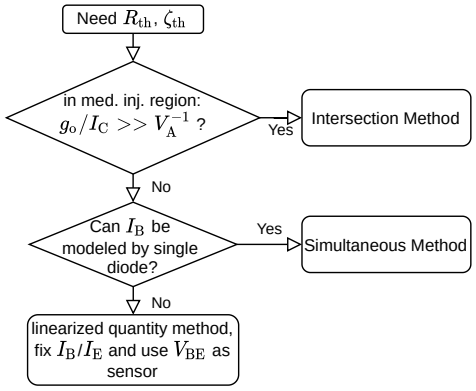

Figure 20: Flowchart including conditions for selecting an R_{th} extraction method in practice.

As discussed earlier, all industry-standard compact models use simplified versions of (1). For minimizing the computational effort during circuit simulation it is

~~required to write $R_{\rm th}$ as a function of the node voltage $T_{\rm j}$-$T_{\rm B}$ of the thermal adjunct network , because a direct $P_{\rm D}$ dependence would lead to additional entries in the circuit Jacobian related to the stamp of $R_{\rm th}$.~~

~~From (1) and $P_{\rm D} = (T_{\rm j} - T_{\rm B})/R_{\rm th}(T_{\rm B}, T_{\rm j})$ one obtains which is a quadratic equation for $R_{\rm th}(T_{\rm B}, T_{\rm j})$ with the solution where $R_{\rm th}(T_{\rm B})$ is given by (2). This formulation is computationally efficient since it generates a simple additional derivative w.r.t. the thermal node voltage only.~~

As shown before, the model parameter $\alpha_{\rm pD}$ is difficult to determine with reasonable accuracy, even from synthetic data. Therefore one may use (3) in practice for estimating $\alpha_{\rm pD}$ as $\zeta_{\rm th} R_{\rm th}(T_{\rm B})/2T_{\rm B}$. The parameter extraction effort is then reduced compared to (5).

VII. Conclusion

A comprehensive and detailed study of commonly used $R_{\rm th}$ extraction methods has been presented. The methods have been applied to various SiGe and InP HBT technologies. It was found that the accuracy of all methods is strongly bias and technology-dependent. Furthermore, ~~there exists~~none of the investigated methods works under all possible circumstances. Based on the obtained results, a guide for method selection in practice has been provided.

~~Finally, a new computationally efficient and more rigorous equation for modeling $R_{\rm th}$ as a function of backside and junction temperature in a compact model has been proposed. Its runtime and convergence performance still needs to be investigated in more detail.~~

For low and cryogenic temperatures, different model equations apply and the methods need to be evaluated again.

Appendix - Differential Methods

From (4), (6) and (8) one can derive the following relations:

$$\left.\frac{\mathrm{d}T_{\rm j}}{\mathrm{d}T_{\rm B}}\right|_{V_{\rm CE}} = \frac{1 + \left.\frac{\mathrm{d}R_{\rm th}}{\mathrm{d}T_{\rm B}}\right|_{V_{\rm CE}} P_{\rm D}}{1 - R_{\rm th} V_{\rm CE} \left.\frac{\mathrm{d}I_{\rm C}}{\mathrm{d}T_{\rm j}}\right|_{V_{\rm CE}}} \approx \frac{1}{1 - R_{\rm th} V_{\rm CE} \left.\frac{\mathrm{d}I_{\rm C}}{\mathrm{d}T_{\rm j}}\right|_{V_{\rm CE}}}, \tag{22}$$

$$\left.\frac{\mathrm{d}T_{\rm j}}{\mathrm{d}V_{\rm CE}}\right|_{T_{\rm B}} = \frac{R_{\rm th} I_{\rm C} \left(1 + V_{\rm CE}/V_{\rm A}\right)}{1 - R_{\rm th} V_{\rm CE} \left.\frac{\mathrm{d}I_{\rm C}}{\mathrm{d}T_{\rm j}}\right|_{T_{\rm B}}}, \tag{23}$$

$$\left.\frac{\mathrm{d}T_{\rm j}}{\mathrm{d}T_{\rm B}}\right|_{P_{\rm D}} = 1 + \left.\frac{\mathrm{d}R_{\rm th}}{\mathrm{d}T_{\rm B}}\right|_{P_{\rm D}} P_{\rm D} \approx 1, \tag{24}$$

$$\left.\frac{\mathrm{d}T_{\rm j}}{\mathrm{d}P_{\rm D}}\right|_{T_{\rm B}} = R_{\rm th} + \left.\frac{\mathrm{d}R_{\rm th}}{\mathrm{d}P_{\rm D}}\right|_{T_{\rm B}} P_{\rm D} \approx R_{\rm th}\left(T_{\rm B}, P_{\rm D}\right). \tag{25}$$

Note that the $P_{\rm D}$ and $T_{\rm B}$ related partial derivatives of the $R_{\rm th}\left(P_{\rm D}, T_{\rm B}\right)$ relation need to be neglected in order to obtain (22), (24) and (25). Up to this point, the Early-effect is taken into account.

Let X be the temperature sensor variable that is a function of $T_{\rm j}$ and $V_{\rm CE}$. Then, using (23) and writing

$$\left.\frac{\mathrm{d}X}{\mathrm{d}V_{\rm CE}}\right|_{T_{\rm B}} = \left(\frac{\mathrm{d}X}{\mathrm{d}T_{\rm j}}\frac{\mathrm{d}T_{\rm j}}{\mathrm{d}V_{\rm CE}}\right)\Bigg|_{T_{\rm B}} = \left.\frac{\mathrm{d}X}{\mathrm{d}T_{\rm j}}\right|_{T_{\rm B}} \frac{R_{\rm th} I_{\rm C}\left(1 + V_{\rm CE}/V_{\rm A}\right)}{1 - R_{\rm th} V_{\rm CE} \left.\frac{\mathrm{d}I_{\rm C}}{\mathrm{d}T_{\rm j}}\right|_{T_{\rm B}}} \tag{26}$$

as well as using (22) and writing

$$\left.\frac{\mathrm{d}X}{\mathrm{d}T_{\rm B}}\right|_{V_{\rm CE}} = \left(\frac{\mathrm{d}X}{\mathrm{d}T_{\rm j}}\frac{\mathrm{d}T_{\rm j}}{\mathrm{d}T_{\rm B}}\right)\Bigg|_{V_{\rm CE}} = \left.\frac{\mathrm{d}X}{\mathrm{d}T_{\rm j}}\right|_{V_{\rm CE}} \frac{1}{1 - R_{\rm th} V_{\rm CE} \left.\frac{\mathrm{d}I_{\rm C}}{\mathrm{d}T_{\rm j}}\right|_{V_{\rm CE}}} \tag{27}$$

yields the generalized version of (7) in [18]. Similarly, from (24), (25) one gets (20), the generalized version of (4) in [19].

Acknowledgment

This work has been partially supported by the German National Science Foundation (DFG SCHR695/16, SCHR695/17, SCHR695/21). The authors like to thank Dr. K. Aufinger (Infineon AG, Germany) and Drs. D. Howard and E. Preisler (Tower Semiconductor, USA) for providing access to B11 and SBC18H5 hardware, and Dr. P. Zampardi (Qorvo, USA) for discussions.

References

[1] M. Schröter and A. Chakravorty, Compact Hierarchical Modeling of Bipolar Transistors with HICUM (Series on Adv. Sol.-State Electron. and Techn.). World Scientific, 2010.

[2] R. Van Der Toorn, J. C. Paasschens, W. J. Kloosterman and H. C. De Graaff, "Mextram", Compact Model. Princ. Tech. Appl. 2010, pp. 199–230.

[3] C. C. McAndrew et al., "VBIC95, the vertical bipolar inter-company model", IEEE J. Solid-State Circuits, vol. 31, no. 10, pp. 1476–1482, 1996.

[4] B. Senapati and C. K. Maiti, "Advanced SPICE modelling of SiGe HBTs using VBIC model", IEE Proc. Circuits, Devices Syst., vol. 149, no. 2, pp. 129–135, 2002.

[5] H. Tran, M. Schröter, D. J. Walkey, D. Marchesan and T. J. Smy, "Simultaneous extraction of thermal and emitter series resistances in bipolar transistors", Proc. IEEE Bipolar/BiCMOS Circuits Technol. Meet., 1997, pp. 170–173.

[6] M. Pfost, V. Kubrak and P. Brenner, "A practical method to extract the thermal resistance for heterojunction bipolar transistors", Eur. Solid-State Device Res. Conf., IEEE, 2003, pp. 335–338.

[7] A. Pawlak, S. Lehmann and M. Schröter, "A simple and accurate method for extracting the emitter and thermal resistance of BJTs and HBTs", Proc. IEEE Bipolar/BiCMOS Circuits Technol. Meet., 2014, pp. 175–178.

[8] W. Liu and A. Yuksel, "Measurement of Junction Temperature of an AlGaAs/GaAs Heterojunction Bipolar Transistor Operating at Large Power Densities", IEEE Trans. Electron Devices, vol. 42, no. 2, pp. 358–360, 1995.

[9] B. Yeats, "Inclusion of topside metal heat spreading in the determination of HBT temperatures by electrical and geometrical methods", Tech. Dig. - GaAs IC Symp., 1999, pp. 59–62.

[10] S. P. Marsh, "Direct extraction technique to derive the junction temperature of HBT's under high self-heating bias conditions", IEEE Trans. Electron Devices, vol. 47, no. 2, pp. 288–291, 2000.

[11] J. Berkner, "Extraction of thermal resistance and its temperature dependence using DC methods", HICUM Workshop, Dresden, 2007.
[12] S. Balanethiram, R. D'Esposito, S. Fregonese, T. Zimmer, J. Berkner and D. Celi, "Extracting the temperature dependence of thermal resistance from temperature-controlled DC measurements of SiGe HBTs", Proc. IEEE Bipolar/BiCMOS Circuits Technol. Meet., 2017, pp. 94–97.
[13] Z. Huszka, K. Nidhin, D. Celi and A. Chakravorty, "Extraction of compact static thermal model parameters for SiGe HBTs", IEEE Trans. Electron Devices, vol. 68, no. 2, pp. 491–496, 2021.
[14] D. E. Dawson, A. K. Gupta and M. L. Salib, "CW measurement of HBT thermal resistance", IEEE Trans. Electron Devices, vol. 39, no. 10, pp. 2235–2239, 1992.
[15] R. Menozzi, J. Barrett and P. Ersland, "A new method to extract HBT thermal resistance and its temperature and power dependence", IEEE Trans. Device Mater. Reliab., vol. 5, no. 3, pp. 595–601, 2005.
[16] V. d'Alessandro, G. Sasso, N. Rinaldi and K. Aufinger, "Influence of scaling and emitter layout on the thermal behavior of toward-THz SiGe:C HBTs", IEEE Trans. Electron Devices, vol. 61, no. 10, pp. 3386–3394, 2014.
[17] V. d'Alessandro, "Experimental DC extraction of the thermal resistance of bipolar transistors taking into account the Early effect", Solid State Electron., vol. 127, pp. 5–12, 2017.
[18] D. T. Zweidinger, R. M. Fox, S. G. Lee and T. Jung, "Extraction of thermal parameters for bipolar circuit simulation", Proc. IEEE Bipolar/BiCMOS Circuits Technol. Meet., 1995, pp. 78–81.
[19] N. Bovolon, P. Baureis, J. E. Müller, P. Zwicknagl, R. Schultheis and E. Zanoni, "A simple method for the thermal resistance measurement of AlGaAs/GaAs heterojunction bipolar transistors", IEEE Trans. Electron Devices, vol. 45, no. 8, pp. 1846–1848, 1998.
[20] F. Korndörfer, "Zum thermischen Widerstand von Silicium-Germanium-Hetero-Bipolartransistoren", Ph.D. dissertation, TU Chemnitz, 2013.
[21] J. R. Waldrop, K. C. Wang and P. M. Asbeck, "Determination of Junction Temperature in AIGaAs/ GaAs Heterojunction Bipolar Transistors by Electrical Measurement", IEEE Trans. Electron Devices, vol. 39, no. 5, pp. 1248–1250, 1992.
[22] J. S. Rieh, D. Greenberg, B. Jagannathan, G. Freeman and S. Subbanna, "Measurement and modeling of thermal resistance of high speed SiGe heterojunction bipolar transistors", Top. Meet. Silicon Monolith. Integr. Circuits RF Syst., 2001, pp. 110–113.
[23] D. J. Walkey, T. J. Smy, T. Macelwee and M. Maliepaard, "Compact representation of temperature and power dependence of thermal resistance in Si, InP and GaAs substrate devices using linear models", Solid-State El2ectronics, vol. 46, no. 6, pp. 819–826, 2002.
[24] J. Paasschens, S. Harmsma and R. van der Toom, "Dependence of thermal resistance on ambient and actual temperature", Bipolar/BiCMOS Cir. Tech. Meet., IEEE, 2004, pp. 96–99.
[25] S. Yadav and A. Chakravorty, "A pragmatic approach to modeling self-heating effects in SiGe HBTs", IEEE Trans. Electron Devices, vol. 64, no. 12, pp. 4844–4849, 2017.
[26] A. K. Sahoo, S. Fregonese, M. Weiss, C. Maneux and T. Zimmer, "A scalable model for temperature dependent thermal resistance of SiGe HBTs", 2013 IEEE Bipolar/BiCMOS Circuits Technol. Meet., IEEE, 2013, pp. 29–32.
[27] T. Rosenbaum, "Performance prediction of a future silicon-germanium heterojunction bipolar transistor technology using a heterogeneous set of simulation tools and approaches", Ph.D. dissertation, TU Dresden, Dresden, 2017.
[28] T. Nardmann, Physics-based compact modeling and parameter extraction for InP heterojunction bipolar transistors with special emphasis on material-specific physical effects and geometry scaling. Books on Demand, 2017.
[29] A. Pawlak, "Advanced modeling of silicon-germanium heterojunction bipolar transistors", Dissertation, TU Dresden, 2015.
[30] N. Rinaldi and V. d'Alessandro, "Theory of electrothermal behavior of bipolar transistors: Part I - Single-finger devices", IEEE Trans. Electron Devices, vol. 52, no. 9, pp. 2009–2021, 2005.
[31] J. Krause and M. Schröter, "Methods for determining the emitter resistance in SiGe HBTs: A review and an evaluation across technology generations", IEEE Trans. Electron Devices, vol. 62, no. 5, pp. 1363–1374, 2015.
[32] M. Schroter et al., "SiGe HBT technology: Future trends and TCAD-based roadmap", Proc. IEEE, vol. 105, no. 6, pp. 1068–1086, 2017.
[33] M. Muller, M. Schroter, C. Jungemann and C. Weimer, "Augmented Drift-Diffusion Transport for the Simulation of Advanced SiGe HBTs", 2019 IEEE BiCMOS Compd. Semicond. Integr. Circuits Technol. Symp., 2022, pp. 1–4.
[34] K. Krattenmacher, M. Müller and M. Schröter, DMT - Device-Modeling-Toolkit, HICUM - Workshop, Munich, 2019.
[35] P. Kuthe, M. Müller and M. Schröter, "VerilogAE: An open source Verilog-A compiler for compact model parameter extraction", IEEE J. Electron Devices Soc., vol. 8, pp. 1416–1423, 2020.
[36] N. Nenadovic et al., "Extraction and modeling of self-heating and mutual thermal coupling impedance of bipolar transistors", IEEE J. Solid-State Circuits, vol. 39, no. 10, pp. 1764–1772, 2004.
[37] N. Nenadovic, V. D'Alessandro, L. Nanver, F. Tamigi, N. Rinaldi and J. Slotboom, "A back-wafer contacted silicon-on-glass integrated bipolar process—part II: A novel analysis of thermal breakdown", IEEE Trans. Electron Devices, vol. 51, no. 1, pp. 51–62, 2004.
[38] J. C. Li, D. A. Hitko, M. Sokolich and P. M. Asbeck, "Experimental method to thermally deembed pads from RTH measurements", IEEE Trans. Electron Devices, vol. 53, no. 10, pp. 2540–2544, 2006.